Visual Abstract

Justification of fracture criteria for salt rocks

A. Baryakh, A. Tsayukov
Mining Institute of the Ural Branch of the Russian Academy of Sciences, Russia
bar@mi-perm.ru, http://orcid.org/0000-0003-2737-6166
andrei.tsayukov@mi-perm.ru, http://orcid.org/0000-0002-9982-4776

ABSTRACT. The study of salt rocks deformation and fracture processes is an essential part of mining parameters justification for mineral salt deposits. The results of uniaxial compression tests on large salt rock specimens are presented as a loading curve and diagrams of the transverse-longitudinal displacements at various distances from the side faces. Based on an isotropic elastoplastic model, a multivariant numerical simulation was performed. Its purpose was to select fracture criteria that accurately describe the loading diagram of specimen and its transverse-longitudinal deformations. The following fracture criteria are considered: Tresca with the associated plastic flow rule, the associated and non-associated Mohr-Coulomb, the parabolic analogue of Mohr-Coulomb criterion and the volumetric fracture criterion. Numerical simulation was carried out by the displacement-based finite element method. Three-dimensional hexahedral eight-node isoparametric elements were used for discretization of the solution domain. It has been established that within the elastoplastic model of media the process of uniaxial compression of a large cubic salt rock specimen is adequately described by the linear Mohr-Coulomb fracture criterion with the non-associated plastic flow, as well as by the associated volumetric parabolic yield criterion with the linear isotropic hardening.

KEYWORDS. Salt rocks; Elastoplasticity; Fracture criteria; Mathematical modeling; Finite element method.

OPEN ACCESS

Citation: Baryakh, A., Tsayukov, A, Justification of fracture criteria for salt rocks, Frattura ed Integrità Strutturale, 62 (2022) 585-601.

Received: 03.08.2022
Accepted: 12.09.2022
Online first: 14.09.2022
Published: 01.10.2022

INTRODUCTION

Salt rocks are classified as quasi-plastic geomaterials as they show pronounced rheological properties and specific response to various external impacts [1-4]. The study of their behavior under loading is essential part of the mining parameters justification for mineral salt deposits [5–7].

A significant part of the experimental studies of deformation and fracture processes for salt rocks under various loading conditions is associated with the formulation of their phenomenological models [8–10] and fracture criteria [11, 12]. As a rule, the choice of optimal fracture criteria is limited by a set of representative strength characteristics of the material. Due to structural heterogeneity of salt rocks two indicators are usually used: uniaxial compressive (σ_c) and tensile (σ_t) strength.

In this regard, the strength of salts is mainly described by the linear Mohr-Coulomb criterion [13] or its parabolic analogue [14]. These criteria generally provide an acceptable assessment of the ultimate stress-strain state of salt rocks.
It should be noted that laboratory experiments are rarely used to set up mathematical models describing the stability of mining structures and predicting changes in their state over time. Such studies are a kind of analogue of physical modeling even in the case of non-compliance with the similarity criteria [15].
In [16], for operational control of the inter-chamber pillars state, which ensures the support of an overlying rock strata during mining of salts, it was proposed to use their transverse deformation. By means of mathematical modeling a preliminary estimation of the critical transverse deformation rate for inter-chamber pillars was given. In order to refine the deformation and fracture model for pillars and their parametric support, a series of tests on uniaxial compression of large cubic salt specimens of 300 × 300 × 300 mm in size was carried out [17]. Fine-grained sylvinite from Verkhnekamsk potash deposit was used. Its average grain size was 2-3 mm. The test scheme is shown in Fig. 1a. During the strain-controlled testing under the perfect adhesion the absolute longitudinal deformation was recorded and the displacements in the middle cross section were measured at various distances from the side faces. To study the development of transverse deformations, special deep marks inside the specimen and contour mark on a side face were fixed. Specimen deformations and displacement of marks during testing were controlled using a non-contact three-dimensional optical system Vic-3D from "Correlated Solutions". Horizontal displacements of marks 0, 5, and 10 cm were measured relative to the central point of 15 cm distance from a specimen's side face (Fig. 1a). The absolute longitudinal deformation of specimen corresponded to its height change.
Load-longitudinal deformation and transverse deformation-longitudinal deformations curves at various distances from a side face was obtained based on the test results for large specimens (Fig. 1, b, c). This information provides an experimental basis for formulation of fracture model for a salt specimen.
The purpose of the presented study is to justify fracture criteria and fracture parameters which simultaneously describe the loading diagram of the salt specimen and its transverse-longitudinal deformations (Fig. 1, b, c) by means of multivariant mathematical modeling.

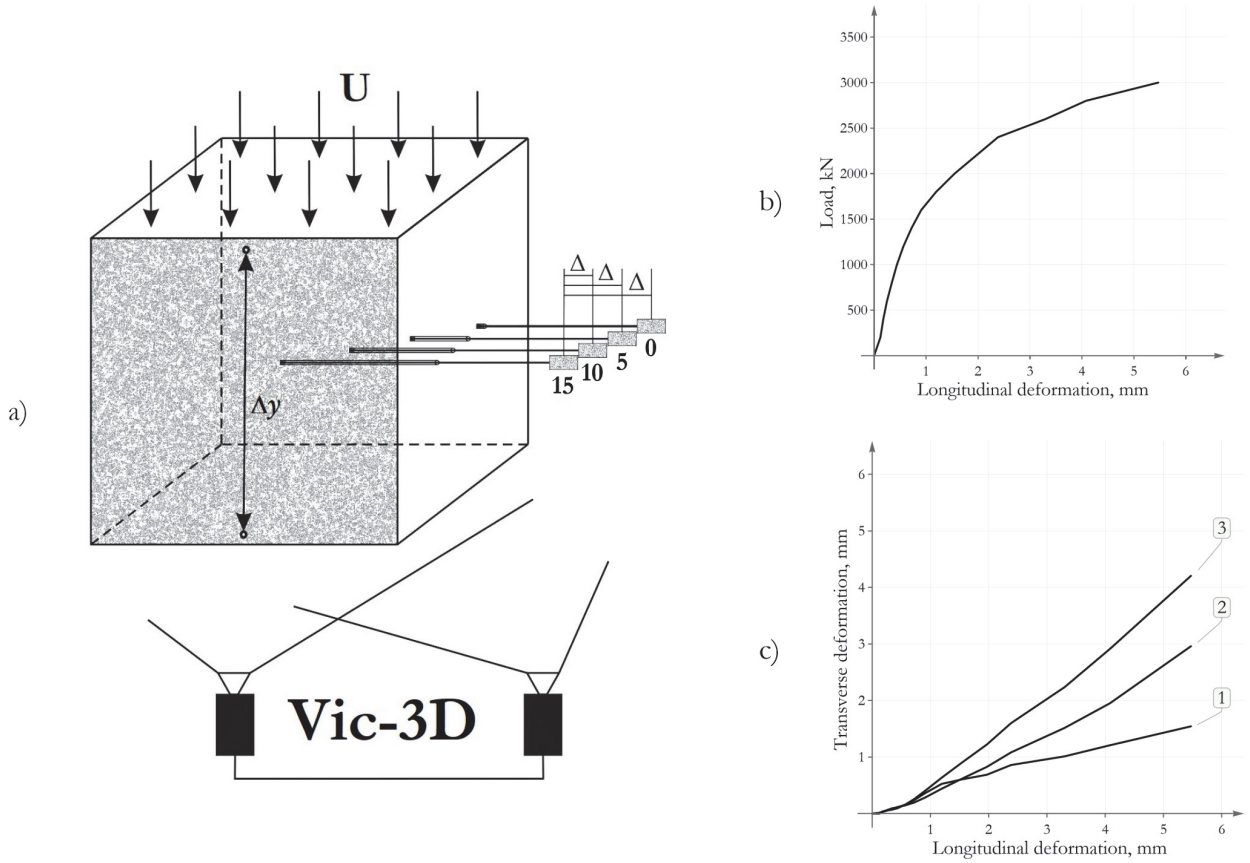

Figure 1: Test scheme for a salt specimen (a), average loading diagram (b) and transverse-longitudinal deformations (c) [17]: 1—0 cm from a side face of the specimen, 2—5 cm from a side face, 3—10 cm from a side face.

MATHEMATICAL MODEL

The mathematical description of salt deformation was based on an isotropic elastoplastic model of media [18]. Elastic straining was described by Hooke's law. The plasticity (yielding) was determined by the yield function

$$\Phi(\sigma,\kappa,\mathbf{A})$$

and plastic flow potential

$$\Psi(\sigma,\kappa,\mathbf{A})$$

In general case, the arguments are: the stress tensor—σ, the isotropic hardening parameter—κ, and a set of material internal state variables and constants—$\mathbf{A}$. The yield surface is defined as

$$\Phi = 0 \tag{1}$$

Plastic straining was described by the evolution equation [19]

$$\dot{\varepsilon}^{\mathrm{p}} = \dot{\lambda}\frac{\partial\Psi}{\partial\sigma} \tag{2}$$

where ε^{p} and λ are the plastic strain tensor and the plastic multiplier, respectively. Associated flow rule states that yield function and plastic potential are identical

$$\Psi \equiv \Phi \tag{3}$$

and the normality condition (Kuhn-Tucker condition) is satisfied [18]. In the case of perfect plasticity, the yield surface (1) does not change its shape. So, only the stress tensor and the set of material constants remain as arguments of (1):

$$\Phi(\sigma,\mathbf{A}) = 0 \tag{4}$$

The implementation of isotropic hardening implied a dimensionless approach (strain hardening) [19], in which the evolution of the parameter κ depends on the evolution of the accumulated plastic strain:

$$\dot{\kappa} = \left\|\dot{\varepsilon}^{\mathrm{p}}\right\| \tag{5}$$

where ||·|| is the Euclidean norm. Only compressive plastic strain was taken into account. No additional response to the plastic tension was assumed. Hence, the evolution of the isotropic hardening parameter is written:

$$\dot{\kappa} = \left\|\dot{\varepsilon}^{\mathrm{p}}_{-}\right\| \tag{6}$$

where the minus sign in the subscript indicates the negative (compressive) part of the plastic strain rate tensor. The positive components vanish. Isotropic hardening of the yield surface was taken into account by internal state variables. In other words, the set of material parameters and constants is a function $\mathbf{A}(\kappa)$, and therefore, $\mathbf{A}(\varepsilon^{\mathrm{p}})$. Thus, the yield surface Eqn. (4) takes the form:

$$\Phi\left(\sigma,\mathbf{A}(\varepsilon^{\mathrm{p}})\right) = 0 \tag{7}$$

The numerical implementation of the mathematical model described above was carried out by the displacement-based finite element method. Three-dimensional hexahedral eight-node isoparametric elements with eight integration points were used

for meshing of the solution domain [19]. The solution domain (300 × 300 × 300 mm) was meshed by cubic elements with 10 mm side.
The boundary conditions corresponded to the performed tests (Fig. 1). On the lower face of cubic specimen, the vertical displacements were fixed (assumed to be zero). Horizontal displacements along the perimeter of the upper and lower faces were constrained as well (the perfect adhesion was observed). Vertical displacements corresponding to the loading conditions were set on the upper face of the specimen.
The elastoplastic relations were solved using the modified Newton-Raphson scheme with a constant stiffness matrix.
Some fracture/plasticity criteria have a plane yield surface representation (e.g., Tresca, Mohr-Coulomb) due to the assumption that the middle principal stress does not contribute to material fracture. In this case, such yield surfaces were described via the multi-surface representation in the principal stress space [18]

$$\bigcup_{i=1}^{n!}\left\{\sigma \mid \Phi_i(\sigma,\mathbf{A})=0,\ \forall j\neq i,\ \Phi_j(\sigma,\mathbf{A})\leq 0\right\} \tag{8}$$

where n is the dimension of the principal stress space. Obviously, at the intersection of yield surfaces, the yield function and the plastic potential lose their continuous differentiability within the general yield surface, and it is impossible to explicitly determine the plastic flow direction. For such kind of singularities, the evolution of plastic strain was represented as a linear combination (Koiter's generalization) [20,21]:

$$\dot{\varepsilon}^{\mathrm{p}}=\sum_i \dot{\lambda}_i \frac{\partial \Psi_i}{\partial \sigma},\quad i=1,2,\ldots,m \tag{9}$$

where m is the number of yield surfaces meeting at the apex/edge of the general yield surface.
Numerical integration of the plastic constitutive relations was performed using the return-mapping algorithm, in particular, the tangent cutting plane (TCP) algorithm [18,20]. Its essence is the linearization of the surface function (7) around the current stress state $\{\sigma^k, \mathbf{A}^k\}$:

$$\begin{aligned}&\Phi(\sigma^k,\mathbf{A}^k)+\tilde{\mathrm{N}}^k:\Delta\sigma+\tilde{\mathbf{K}}^k*\Delta\mathbf{A}=0\\&\tilde{\mathrm{N}}^k=\left.\frac{\partial\Phi}{\partial\sigma}\right|_{\sigma^k,\mathbf{A}^k},\quad \tilde{\mathbf{K}}^k=\left.\frac{\partial\Phi}{\partial\mathbf{A}}\right|_{\sigma^k,\mathbf{A}^k}\end{aligned} \tag{10}$$

where k is the iteration number of TCP algorithm, $\Delta(\cdot)$ is the increment, and $*$ denotes the product of the appropriate type. Using explicit Euler scheme in the context of return-mapping increments the following relations can be obtained

$$\begin{aligned}&\Delta\sigma=\sigma^{k+1}-\sigma^k=-\Delta\lambda\,\mathrm{D}^k:\mathrm{N}^k\\&\Delta\mathbf{A}=\mathbf{A}^{k+1}-\mathbf{A}^k=\Delta\lambda\,\mathbf{H}^k*\mathbf{K}^k\end{aligned} \tag{11}$$

Substitution them into (10) gives the expression for the plastic multiplier increment in closed form:

$$\Delta\lambda=\frac{\Phi^k}{\tilde{\mathrm{N}}^k:\mathrm{D}^k:\mathrm{N}^k-\tilde{\mathbf{K}}^k*\mathbf{H}^k*\mathbf{K}^k} \tag{12}$$

In general, D denotes the fourth-order elasticity tensor (D^k = const, since the modified Newton-Raphson scheme is used), $\mathbf{H}$ is the generalized hardening modulus, $\mathrm{N}=\partial\Psi/\partial\sigma$ is the plastic flow direction, $\mathbf{K}$ is the generalization of the isotropic hardening parameter κ. For the associated plastic flow, $\tilde{\mathrm{N}}$ and N coincide. Substitution (12) in (11) allows us to determine the new stress state $\{\sigma^{k+1}, \mathbf{A}^{k+1}\}$. TCP algorithm starts from the trial solution at $k=0$

$$\{\sigma^0,\mathbf{A}^0\}=\{\sigma^{\mathrm{trial}},\mathbf{A}^{\mathrm{trial}}\} \tag{13}$$

The iterative process continues until the convergence condition is satisfied

$$\Phi(\sigma^k, \mathbf{A}^k) \le \delta \tag{14}$$

where δ is a prescribed positive value close to zero. It should be noted that for linear yield surfaces, single iteration is sufficient for the TCP algorithm to be converged. The multi-surface representation (8) and the corresponding plastic flow vector (9) lead to the solution of m Eqns. (10) for λ within single iteration.
The spectral decomposition of the symmetric stress tensor [18] is used for convenience of applying the return-mapping algorithm

$$\sigma = \sum_{j=1}^{p} \sigma_j \mathbf{E}_j \tag{15}$$

where σ_j are the principal stresses (eigenvalues), $\mathbf{E}_j$ are the corresponding eigenprojections, and p is the number of distinct eigenvalues.

YIELD CRITERIA

Tresca criterion

The Tresca strength criterion [18, 20] is mainly used to describe the plastic straining of metals and, a priori, is not suitable for rocks. Here, it is analyzed only for comparative purposes.
In the principal stress space, the Tresca criterion is written as:

$$\tau_y = \frac{1}{2}(\sigma_{\max} - \sigma_{\min}) \tag{16}$$

where $\sigma_{\max}$ and $\sigma_{\min}$ are the major and minor principal stresses, respectively, and τ_y is the shear yield stress. Here and below the tensile stress is implied to be positive. Expression (16) can also be written as a yield function:

$$\Phi(\sigma, \sigma_y) = \sigma_{\max} - \sigma_{\min} - \sigma_y \tag{17}$$

where $\sigma_y = 2\tau_y$ is the uniaxial yield stress. The set $\mathbf{A}$ here contains the single parameter σ_y, which denotes the material strength. In this case, the uniaxial compression strength σ_c was assumed as the yield strength. The Tresca yield surface is shown in Fig. 2. The multi-surface representation reads:

$$\begin{aligned}
\Phi_1(\sigma, \sigma_c) &= \sigma_1 - \sigma_3 - \sigma_c \\
\Phi_2(\sigma, \sigma_c) &= \sigma_2 - \sigma_3 - \sigma_c \\
\Phi_3(\sigma, \sigma_c) &= \sigma_2 - \sigma_1 - \sigma_c \\
\Phi_4(\sigma, \sigma_c) &= \sigma_3 - \sigma_1 - \sigma_c \\
\Phi_5(\sigma, \sigma_c) &= \sigma_3 - \sigma_2 - \sigma_c \\
\Phi_6(\sigma, \sigma_c) &= \sigma_1 - \sigma_2 - \sigma_c
\end{aligned} \tag{18}$$

The spectral decomposition (15) allows the consideration to be concentrated on the sextant $\sigma_1 > \sigma_2 > \sigma_3$. So, only three surfaces from (18) can be used in the return-mapping algorithm—Φ_1, Φ_2, Φ_6. The choice of the target edge ($\Phi_{1\wedge2}$ or $\Phi_{1\wedge6}$) in case of the yielding from the edge of the yield surface was performed using the approach proposed in [18]. The associated plastic flow was accepted. The corresponding parameters of the TCP algorithm in the principal stress space are:

$$\begin{aligned}\tilde{\mathrm{N}}_1^T &= \mathrm{N}_1^T = \begin{pmatrix}1 & 0 & -1\end{pmatrix}\\ \tilde{\mathrm{N}}_2^T &= \mathrm{N}_2^T = \begin{pmatrix}0 & 1 & -1\end{pmatrix}\\ \tilde{\mathrm{N}}_6^T &= \mathrm{N}_6^T = \begin{pmatrix}1 & -1 & 0\end{pmatrix}\end{aligned} \tag{19}$$

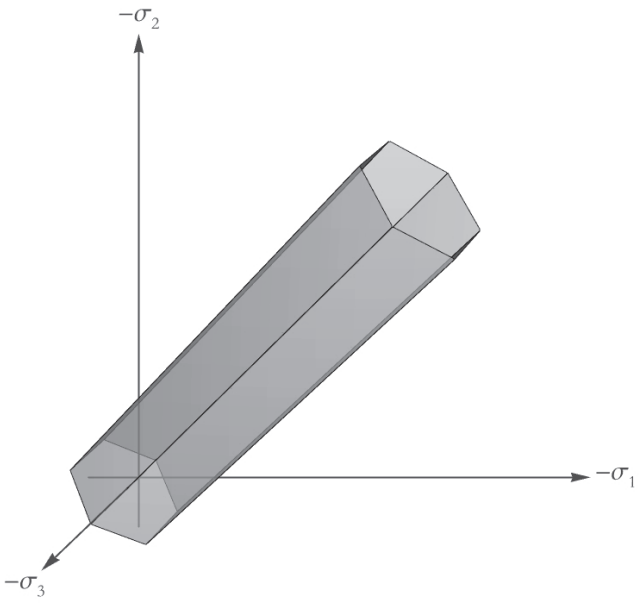

Figure 2: The Tresca yield surface.

Since set **A** for the Tresca criterion consists of single element σ_c, the hardening was implemented by its variation. For simplicity, the linear relation is assumed

$$\mathbf{A}(\varepsilon^{\mathrm{p}}) = \sigma_c(\varepsilon^{\mathrm{p}}) = \sigma_{c,0} + h\varepsilon^{\mathrm{p}} \tag{20}$$

where $\sigma_{c,0}$ is the initial uniaxial compression strength, and h is the hardening modulus of stress dimension. Thus, the TCP algorithm parameters associated with hardening take the form:

$$\begin{aligned}\tilde{\mathbf{K}} &= -1\\ \mathbf{H} &= h\\ \mathbf{K} &= \left\|\mathrm{N}_-\right\|\end{aligned} \tag{21}$$

The results of numerical simulation of the specimen loading, based on the associated Tresca yield criterion, are shown in Fig. 3. The selected mechanical and criterion parameters are presented in Tab. 1.

Young's modulus, GPa	Poisson's ratio	Uniaxial compressive strength, MPa	Hardening modulus, GPa
6.7	0.3	22	0.6

Table 1: Salt specimen parameters (associated Tresca).

It can be seen that the simulated results are in a reasonable agreement with the experimental at the elastic stage, as well as at the plastic one, starting from approximately 2000–2100 kN of load level. As expected, the distribution of transverse deformations over the width of the cubic specimen does not correspond to the test values. According to the associated Tresca plastic flow, insufficient transverse deformations are obtained. This is due to the fact that the Tresca criterion does

not depend on the hydrostatic stress (pressure-insensitive) and plastic flow occurs only in the deviatoric plane. Volumetric plastic strain is neglected.

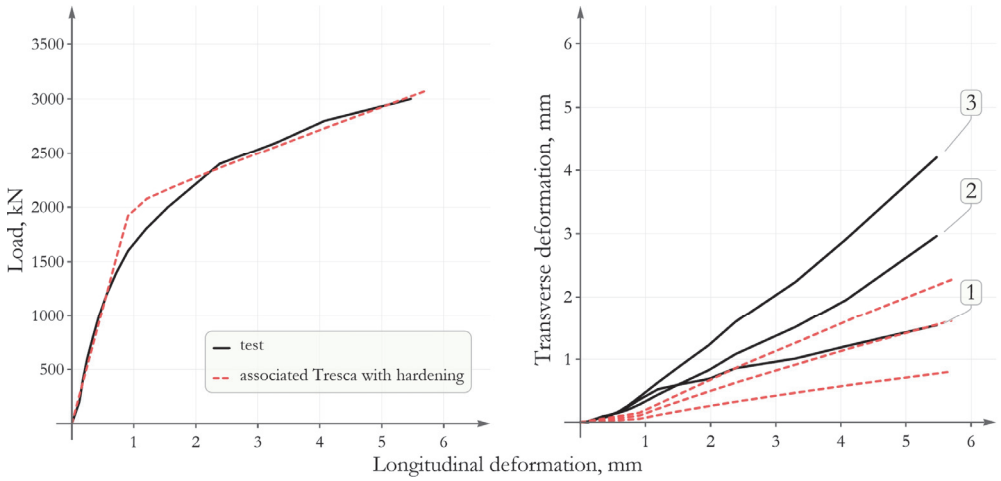

Figure 3: Simulation results (associated Tresca yield criterion with hardening).

Mohr-Coulomb criterion

The classical Mohr-Coulomb yield criterion [13,18,20] is often used to describe the mechanical behavior of soils, rocks, and concrete. Unlike Tresca, the Mohr-Coulomb criterion is pressure-sensitive. In the Mohr axes, the criterion is represented as a linear relation

$$\tau_y = c - \sigma_n \tan\phi \tag{22}$$

In expression (22), τ_y is the shear yield stress, c is the cohesion, ϕ is the frictional angle, and σ_n is the normal stress, a positive value of which indicates tension. The corresponding yield function in the principal stress space is written as:

$$\Phi\left(\sigma,\{c,\phi\}\right) = \sigma_{\max} - \sigma_{\min} + (\sigma_{\max} + \sigma_{\min})\sin\phi - 2c\cos\phi \tag{23}$$

Similar to the Tresca criterion, the Mohr-Coulomb yield surface has a multi-surface representation:

$$\begin{aligned}
\Phi_1\left(\sigma,\{c,\phi\}\right) &= \sigma_1 - \sigma_3 + (\sigma_1 + \sigma_3)\sin\phi - 2c\cos\phi \\
\Phi_2\left(\sigma,\{c,\phi\}\right) &= \sigma_2 - \sigma_3 + (\sigma_2 + \sigma_3)\sin\phi - 2c\cos\phi \\
\Phi_3\left(\sigma,\{c,\phi\}\right) &= \sigma_2 - \sigma_1 + (\sigma_2 + \sigma_1)\sin\phi - 2c\cos\phi \\
\Phi_4\left(\sigma,\{c,\phi\}\right) &= \sigma_3 - \sigma_1 + (\sigma_3 + \sigma_1)\sin\phi - 2c\cos\phi \\
\Phi_5\left(\sigma,\{c,\phi\}\right) &= \sigma_3 - \sigma_2 + (\sigma_3 + \sigma_2)\sin\phi - 2c\cos\phi \\
\Phi_6\left(\sigma,\{c,\phi\}\right) &= \sigma_1 - \sigma_2 + (\sigma_1 + \sigma_2)\sin\phi - 2c\cos\phi
\end{aligned} \tag{24}$$

The set **A** contains two parameters $\{c,\phi\}$. The yield surface in the principal stress space is illustrated in Fig. 4.
For numerical simulation of the salt specimen loading, the plastic flow was assumed to be associated, and the material was perfectly plastic. The corresponding TCP algorithm parameters in principal stresses are:

$$\begin{aligned}
\tilde{\mathrm{N}}_1^T &= \mathrm{N}_1^T = \begin{pmatrix} 1+\sin\varphi & 0 & -1+\sin\varphi \end{pmatrix} \\
\tilde{\mathrm{N}}_2^T &= \mathrm{N}_2^T = \begin{pmatrix} 0 & 1+\sin\varphi & -1+\sin\varphi \end{pmatrix}. \\
\tilde{\mathrm{N}}_6^T &= \mathrm{N}_6^T = \begin{pmatrix} 1+\sin\varphi & -1+\sin\varphi & 0 \end{pmatrix}
\end{aligned} \tag{25}$$

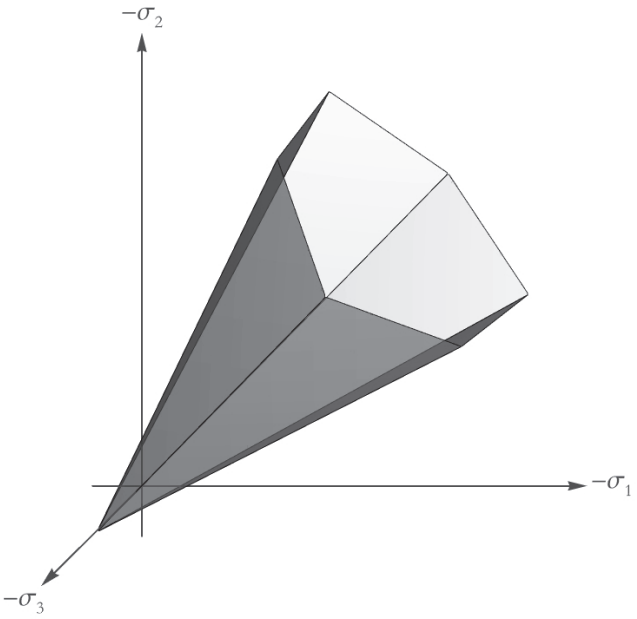

Figure 4: The Mohr-Coulomb yield surface.

It should be noted that volumetric plastic strain rate is positive in this case, i.e. the material is dilatant. All hardening-related parameters of the TCP algorithm are missing.
The results of numerical simulation are illustrated in Fig. 5. The corresponding mechanical and criterion parameters of the simulation are presented in Tab. 2.

Young's modulus, GPa	Poisson's ratio	Cohesion, MPa	Frictional angle, deg
6.7	0.3	4.5	30

Table 2: Salt specimen parameters (associated Mohr-Coulomb)

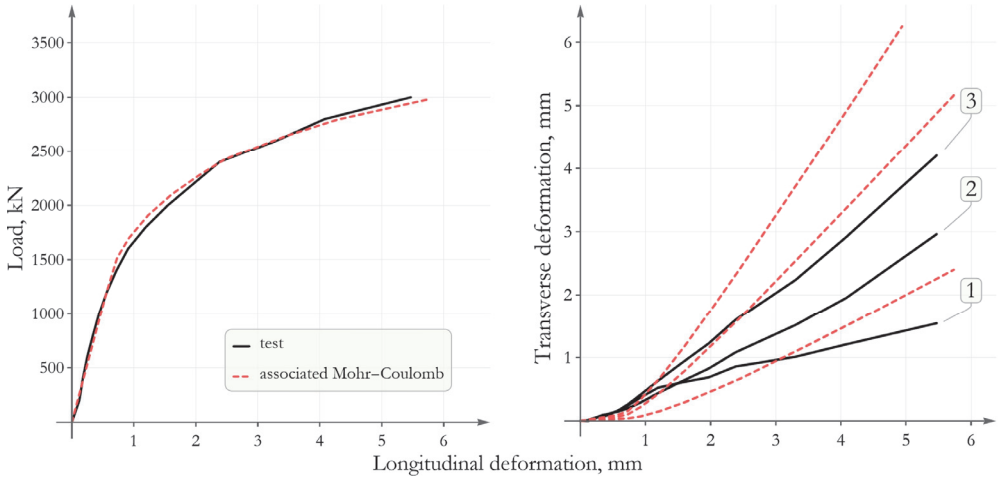

Figure 5: Simulation results (associated Mohr-Coulomb yield criterion).

As can be seen, the simulated loading curve of perfectly plastic straining quite accurately describes all stages of the loading diagram. At the same time, the calculated transverse deformations of the cubic specimen exceed experimental results. This behavior is typical for the associated Mohr-Coulomb plastic flow [8, 12].

This problem is solved by non-associated flow rule. An additional parameter is introduced—the dilatancy angle $\psi < \phi$. In other words, the frictional angle in plastic flow potential is replaced by the dilatancy angle:

$$\Phi(\sigma,\mathbf{A}) = \Phi(\sigma,\{c,\varphi\})$$
$$\Psi(\sigma,\mathbf{A}) = \Phi(\sigma,\{c,\psi\}) \tag{26}$$

Hence, $\tilde{\mathrm{N}} \neq \mathrm{N}$:

$$\tilde{\mathrm{N}}_1^T = \left(1+\sin\varphi \quad 0 \quad -1+\sin\varphi\right), \quad \mathrm{N}_1^T = \left(1+\sin\psi \quad 0 \quad -1+\sin\psi\right)$$
$$\tilde{\mathrm{N}}_2^T = \left(0 \quad 1+\sin\varphi \quad -1+\sin\varphi\right), \quad \mathrm{N}_2^T = \left(0 \quad 1+\sin\psi \quad -1+\sin\psi\right) \tag{27}$$
$$\tilde{\mathrm{N}}_6^T = \left(1+\sin\varphi \quad -1+\sin\varphi \quad 0\right), \quad \mathrm{N}_6^T = \left(1+\sin\psi \quad -1+\sin\psi \quad 0\right)$$

Now, by varying the angle ψ, the dilatancy level is adjusted. The limit case, when $\psi = 0$, means the absence of dilatancy, which corresponds to Tresca's plastic flow.

Young's modulus, GPa	Poisson's ratio	Cohesion, MPa	Frictional angle, deg	Dilatancy angle, deg
6.7	0.3	4	35	18

Table 3: Salt specimen parameters (non-associated Mohr-Coulomb)

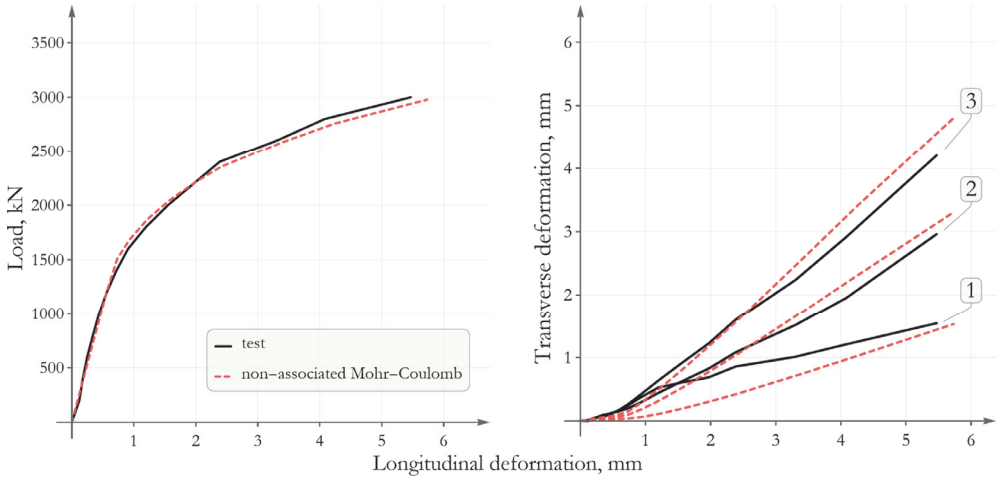

Figure 6: Simulation results (non-associated Mohr-Coulomb yield criterion).

The results of simulation using the non-associated Mohr-Coulomb yield criterion (26) are illustrated in Fig. 6. The selected parameters of the simulation are shown in Tab. 3. It can be seen that the calculated and experimental curves almost coincide. The evolution of transverse deformations qualitatively corresponds to the test.

Parabolic envelope of Mohr circles/Rankine

Recently, the so-called parabolic fracture criteria have become popular. There are a significant number of them [11,12]. Their use is complicated by large number of parameters. One of the frequently applied parabolic criteria in rock strength certificates (including salts) is the parabolic envelope of Mohr circles [14]. It assumes that the Mohr circles under uniaxial compression and tension are tangent to the envelope. In this regard, the criterion has the following form in the Mohr coordinates:

$$p\tau_y^2 = q - \sigma_n \tag{28}$$

where the parabola coefficients are written as

$$p = \frac{1}{r^2 \sigma_t}\left(1+\sqrt{1+r}\right)^2, \quad q = \sigma_t, \quad r = \frac{\sigma_c}{\sigma_t} \tag{29}$$

The parameters of the parabolic criterion are the uniaxial compressive and tensile strengths—σ_c and σ_t. Tensile stresses are positive. The corresponding yield function in the principal stress space can be written as:

$$\begin{aligned} &\Phi^{PMC}\left(\sigma,\{\sigma_c,\sigma_t\}\right) = (\sigma_{\max}-\sigma_{\min})^2 - P(\sigma_c,\sigma_t)(\sigma_{\max}+\sigma_{\min}) - Q(\sigma_c,\sigma_t) \\ &P(\sigma_c,\sigma_t) = -\frac{2}{p} \\ &Q(\sigma_c,\sigma_t) = -\frac{1}{p^2} + 4\frac{q}{p} \end{aligned} \tag{30}$$

The multi-surface representation of criterion (30) has three components

$$\begin{aligned} &\Phi_1^{PMC}\left(\sigma,\{\sigma_c,\sigma_t\}\right) = (\sigma_1-\sigma_3)^2 - P(\sigma_c,\sigma_t)(\sigma_1+\sigma_3) - Q(\sigma_c,\sigma_t) \\ &\Phi_2^{PMC}\left(\sigma,\{\sigma_c,\sigma_t\}\right) = (\sigma_2-\sigma_3)^2 - P(\sigma_c,\sigma_t)(\sigma_2+\sigma_3) - Q(\sigma_c,\sigma_t) \\ &\Phi_3^{PMC}\left(\sigma,\{\sigma_c,\sigma_t\}\right) = (\sigma_1-\sigma_2)^2 - P(\sigma_c,\sigma_t)(\sigma_1+\sigma_2) - Q(\sigma_c,\sigma_t) \end{aligned} \tag{31}$$

since, unlike the linear yield surfaces (17), (23) described above, for parabolic criteria the following relations are valid

$$\begin{aligned} &\Phi_1^{Parabolic} \equiv \Phi_4^{Parabolic} \\ &\Phi_2^{Parabolic} \equiv \Phi_5^{Parabolic} \\ &\Phi_3^{Parabolic} \equiv \Phi_6^{Parabolic} \end{aligned} \tag{32}$$

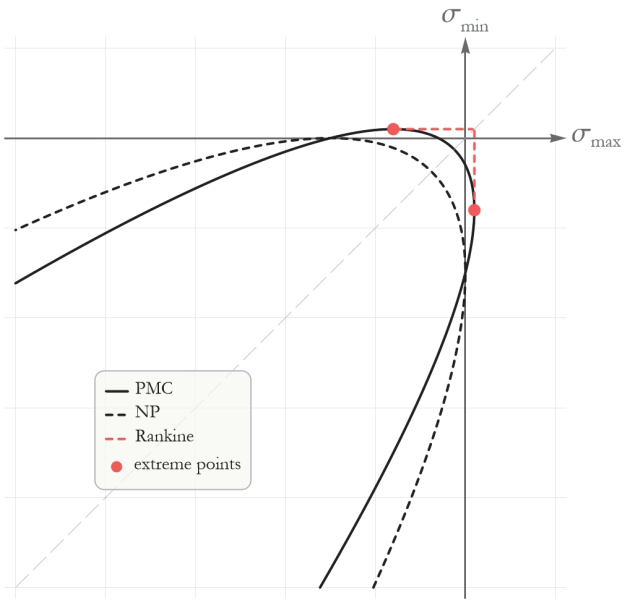

Figure 7: Parabolic envelope of Mohr circles (black solid line), normal parabolic criterion (black dashed line), additional Rankine criterion (red dashed line) and extreme points (red dots) in the principal stress space.

Parabolic criterion (30) has one substantial drawback. In the absence of stresses, the criterion indicates the plastically admissible stress state of the material. This follows from Fig. 7 (black solid line). The interior of the parabola does not include the origin of the principal stress space. This is more clearly seen in the limit case

$$\lim_{\sigma_t \to 0} \Phi^{PMC}\left(\sigma,\{\sigma_c,\sigma_t\}\right) = \\ = \Phi^{NP}\left(\sigma,\sigma_c\right) = (\sigma_{\max} - \sigma_{\min})^2 - 2\sigma_c(\sigma_{\max} + \sigma_{\min}) + \sigma_c^2 \tag{33}$$

The criterion (33) is also known as the normal parabolic criterion [2,4] (black dashed line in Fig. 7). This implies that beyond the extremum of principal stresses (red dots in Fig. 7)

$$\sigma_{\max}, \sigma_{\min} > \frac{1}{2} P(\sigma_c,\sigma_t) + \sigma_t \tag{34}$$

the criterion in the form of a parabolic envelope of Mohr circles has no physical sense.
In this regard, beyond the extreme points (34), the yield surface (30) can be complemented with "cut-offs" limiting tension according to uniaxial tensile strength σ_t. This technique is often used in practice [11]. The condition limiting tensile stresses is known as the Rankine criterion [20,22]

$$\Phi^R(\sigma,\sigma_t) = \sigma_{\max} - \sigma_t \tag{35}$$

The corresponding multi-surface representation is:

$$\begin{aligned} \Phi_1^R(\sigma,\sigma_t) &= \sigma_1 - \sigma_t \\ \Phi_2^R(\sigma,\sigma_t) &= \sigma_2 - \sigma_t \\ \Phi_3^R(\sigma,\sigma_t) &= \sigma_3 - \sigma_t \end{aligned} \tag{36}$$

The set **A** contains one parameter σ_t.

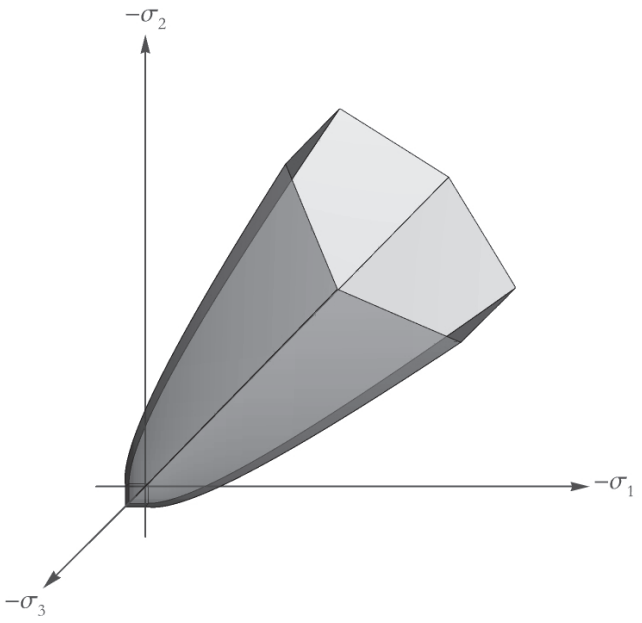

Figure 8: The PMC/R yield surface.

Combining the above, the total yield surface "Parabolic envelope of Mohr circles/Rankine" (PMC/R) can be written as a piecewise function for the sextant $\sigma_{\max} > \sigma_{\mathrm{mid}} > \sigma_{\min}$:

$$\Phi^{PMC/R}(\sigma,\{\sigma_c,\sigma_t\})=\begin{cases}\Phi^{PMC}(\sigma,\{\sigma_c,\sigma_t\}), & \sigma_{\min}\le\dfrac{1}{2}P(\sigma_c,\sigma_t)+\sigma_t\\ \Phi^{R}(\sigma,\sigma_t), & \sigma_{\min}>\dfrac{1}{2}P(\sigma_c,\sigma_t)+\sigma_t\end{cases} \tag{37}$$

where the parabolic criterion (30) describes the "compression-compression" regime of the stress-strain state (SSS) and partly "tension-compression", and the Rankine criterion (35) limits the tensile stresses. The total yield surface (37) is illustrated in Fig. 8. The set **A** for (37) contains two parameters $\{\sigma_c,\ \sigma_t\}$.

The numerical simulation of uniaxial loading of a cubic salt specimen was carried out implying the associated law of plastic strain. The corresponding parameters of the TCP algorithm in principal stresses for the parabolic envelope of Mohr circles are:

$$\begin{aligned}&\left(\tilde{\mathrm{N}}_1^{PMC}\right)^T=\left(\mathrm{N}_1^{PMC}\right)^T=\left(a_{1,3}\quad 0\quad b_{1,3}\right)\\ &\left(\tilde{\mathrm{N}}_2^{PMC}\right)^T=\left(\mathrm{N}_2^{PMC}\right)^T=\left(0\quad a_{2,3}\quad b_{2,3}\right)\\ &\left(\tilde{\mathrm{N}}_3^{PMC}\right)^T=\left(\mathrm{N}_3^{PMC}\right)^T=\left(a_{1,2}\quad b_{1,2}\quad 0\right)\\ &a_{\max,\min}=\ 2(\sigma_{\max}-\sigma_{\min})-P(\sigma_c,\sigma_t)\\ &b_{\max,\min}=-2(\sigma_{\max}-\sigma_{\min})-P(\sigma_c,\sigma_t)\end{aligned} \tag{38}$$

Also for the Rankine criterion they can be written as:

$$\begin{aligned}&\left(\tilde{\mathrm{N}}_1^{R}\right)^T=\left(\mathrm{N}_1^{R}\right)^T=\left(1\quad 0\quad 0\right)\\ &\left(\tilde{\mathrm{N}}_2^{R}\right)^T=\left(\mathrm{N}_2^{R}\right)^T=\left(0\quad 1\quad 0\right)\\ &\left(\tilde{\mathrm{N}}_3^{R}\right)^T=\left(\mathrm{N}_3^{R}\right)^T=\left(0\quad 0\quad 1\right).\end{aligned} \tag{39}$$

Similar to the linear Mohr-Coulomb criterion (22), the material is also dilatant. The linear isotropic hardening was incorporated. Hardening was implemented by evolution of the uniaxial compressive strength similar to the Tresca criterion (20). Clearly, this effect works only in the region where the parabolic criterion (30) is satisfied. The TCP algorithm parameters associated with the hardening are:

$$\begin{aligned}&\tilde{\mathbf{K}}=-(\sigma_{\max}-\sigma_{\min})\frac{\partial P}{\partial\sigma_c}-\frac{\partial Q}{\partial\sigma_c}\\ &\mathbf{H}=h\\ &\mathbf{K}=\left\|\mathrm{N}_{-}^{PMC}\right\|\end{aligned} \tag{40}$$

The derivatives in expression $(40)_1$ can be written using the chain rule:

$$\begin{aligned}&\frac{\partial P}{\partial\sigma_c}=\frac{\partial P}{\partial p}\frac{\partial p}{\partial r}\frac{\partial r}{\partial\sigma_c}\\ &\frac{\partial Q}{\partial\sigma_c}=\frac{\partial Q}{\partial p}\frac{\partial p}{\partial r}\frac{\partial r}{\partial\sigma_c}\end{aligned} \tag{41}$$

Partial derivatives are written in the following form:

$$\frac{\partial P}{\partial p}=\frac{2}{p^2},\quad \frac{\partial Q}{\partial p}=\frac{2-4pq}{p^3},\quad \frac{\partial p}{\partial r}=-\frac{\left(1+\sqrt{1+r}\right)\left(r+2\left[1+\sqrt{1+r}\right]\right)}{r^3 q\sqrt{1+r}},\quad \frac{\partial r}{\partial \sigma_c}=\frac{1}{q} \tag{42}$$

Young's modulus, GPa	Poisson's ratio	Uniaxial compressive strength, MPa	Uniaxial tensile strength, MPa	Hardening modulus, GPa
6.7	0.3	16	1	0.23

Table 4: Salt specimen parameters (associated PMC/R)

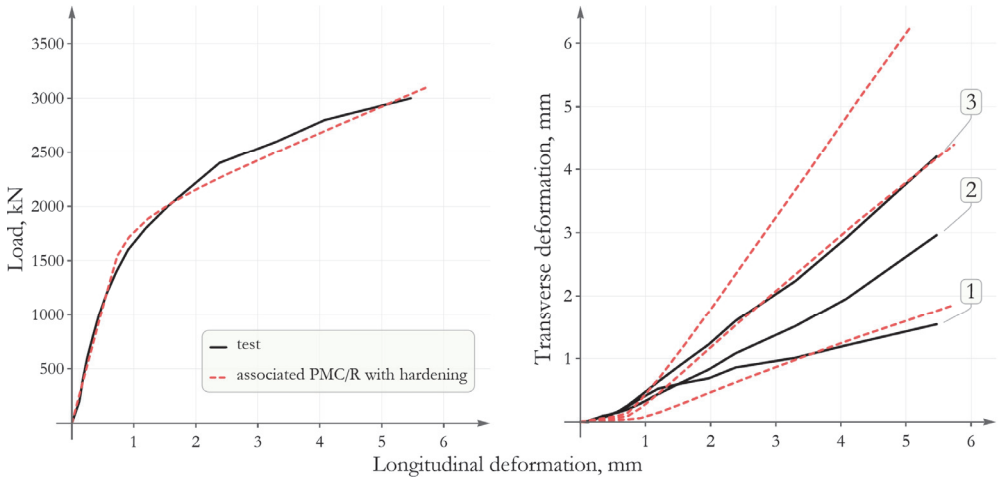

Figure 9: Simulation results (associated PMC/R yield criterion).

It is impossible to constrain the excess of transverse deformations by adopting a non-associated law of plastic flow for the PCM/R criterion, since this can only be done by taking a compressive strength lower than the initial one, which has no physical sense.
The results of multivariant numerical simulations are illustrated in Fig. 9. The obtained simulation parameters are shown in Tab. 4.

Volumetric strength criterion [23]

Another interesting parabolic fracture criterion of rocks was proposed in [23]. The criterion assumes that the fracture of the material occurs due to shear and tear, similar to the Mohr-Coulomb and PMC/R criteria. However, as a characteristic of shear strength the shear stress intensity is used, and as a characteristic of tear strength, the normal stresses described by a spherical tensor are applied. The rock strength criterion has the form:

$$\sigma_i^2 = b - a\mathbf{I}(\sigma) \tag{43}$$

where σ_i is the shear stress intensity, $\mathbf{I}(\sigma)$ is the first invariant of the stress tensor, and the coefficients a and b are determined from uniaxial compression and tensile tests as:

$$\begin{aligned} a &= \sigma_c - \sigma_t \\ b &= \sigma_c \sigma_t \end{aligned} \tag{44}$$

The yield function in the principal stress space is written as:

$$\Phi\left(\sigma,\{\sigma_c,\sigma_t\}\right)=\frac{1}{2}\left[(\sigma_1-\sigma_2)^2+(\sigma_2-\sigma_3)^2+(\sigma_3-\sigma_1)^2\right]+(\sigma_c-\sigma_t)(\sigma_1+\sigma_2+\sigma_3)-\sigma_c\sigma_t \tag{45}$$

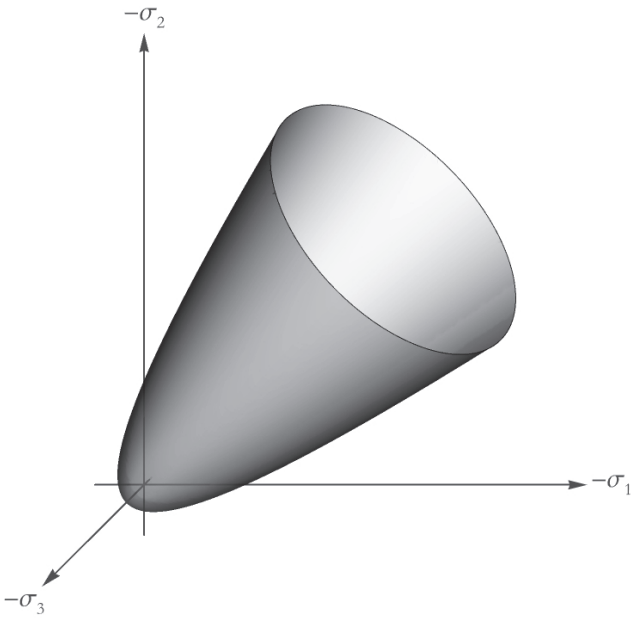

Figure 10: The yield surface of criterion [23].

The strength criterion (45) is volumetric, since it includes the influence of the middle stress. The multi-surface representation is not necessary. The yield surface is continuously differentiable. The set **A** for (45) also consists of two parameters $\{\sigma_c, \sigma_t\}$. A graphical representation of the yield surface is shown in Fig. 10. The yield surface is a paraboloid of revolution around the hydrostatic axis $\sigma_1 = \sigma_2 = \sigma_3$.

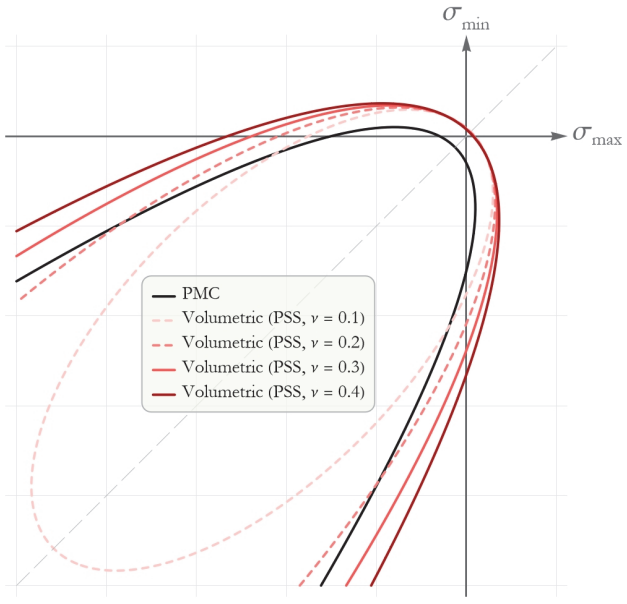

Figure 11: The comparison of PMC and parabolic criteria [23] for PSS.

In contrast to the PMC criterion (30), the criterion [23] (45) has a physical sense in all SSS regimes, since the origin of the coordinates of the principal stress space is in the interior of the yield surface. Comparison of two criteria is shown in Fig. 11 for plane-strain state (PSS). PSS form of the criterion [23] is obtained by replacing the middle principal stress by the

expression $\sigma_2 = \nu(\sigma_1 + \sigma_3)$, where ν is the Poisson's ratio and $\sigma_1 = \sigma_{\max}$, $\sigma_3 = \sigma_{\min}$. The PSS yield surface of the criterion [23] is an ellipse, the size of which depends on the Poisson's ratio. Fig. 11 shows the yield surfaces of the criterion [23] for some ν coefficients. For values of $\nu = [0.3, 0.4]$, the yield surfaces in the largest range of principal stresses are similar to the PMC criterion.

The numerical simulation of the uniaxial loading of a cubic salt specimen was carried out implying the associated plastic flow rule. The corresponding TCP algorithm parameters in the principal stresses for the criterion [23] are determined by:

$$\tilde{\mathrm{N}} = \mathrm{N} = \begin{pmatrix} 2\sigma_1 - \sigma_2 - \sigma_3 + \sigma_c - \sigma_t \\ 2\sigma_2 - \sigma_1 - \sigma_3 + \sigma_c - \sigma_t \\ 2\sigma_3 - \sigma_1 - \sigma_2 + \sigma_c - \sigma_t \end{pmatrix} \tag{46}$$

The effect of volume increase (dilatancy) is reflected in the model. The linear isotropic hardening is adopted. Hardening was implemented similar to (20) by varying the uniaxial compressive strength σ_c. Hardening-related parameters of the TCP algorithm are written as:

$$\begin{aligned} \tilde{\mathbf{K}} &= \sigma_1 + \sigma_2 + \sigma_3 - \sigma_t \\ \mathbf{H} &= h \\ \mathbf{K} &= \|\mathrm{N}_-\| \end{aligned} \tag{47}$$

The results of multivariant numerical simulation are shown in Fig. 12. The parameters of model and fracture criterion are presented in Tab. 5.

Young's modulus, GPa	Poisson's ratio	Uniaxial compressive strength, MPa	Uniaxial tensile strength, MPa	Hardening modulus, GPa
6.7	0.3	14	1	0.35

Table 5: Salt specimen parameters (associated volumetric yield criterion)

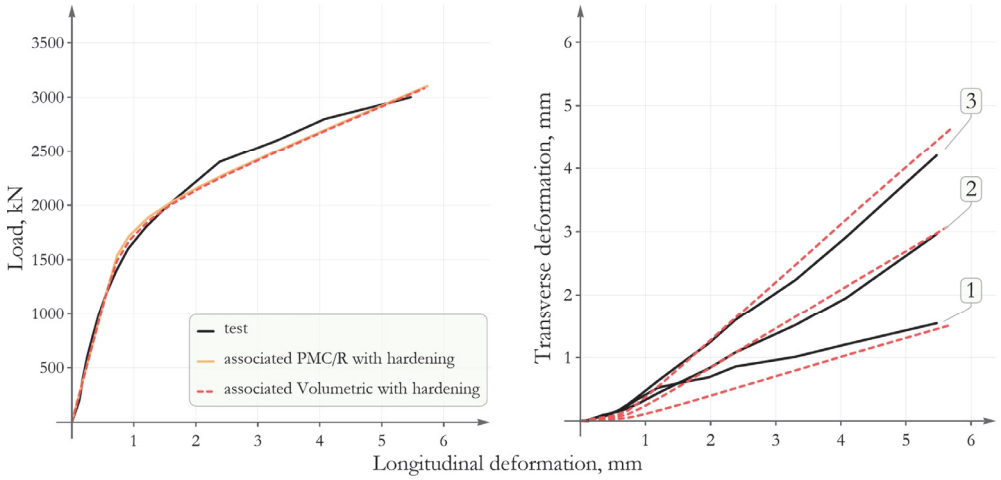

Figure 12: Simulation results (associated volumetric yield criterion).

The simulation results show good agreement between the calculated and experimental loading curves. The resulting loading diagram for the criterion [23] very close to the curve for PMC/R. However, in contrast to PMC/R, the criterion [23] gives much better correspondence with the test data on the transverse-longitudinal deformations and provides a more adequate description of the uniaxial deformation process for a cubic salt specimen.

Conclusion

Some fracture criteria are considered within the framework of elastoplastic model for uniaxial deformation of a large cubic salt rock specimen.

As expected, the Tresca strength criterion and the associated plastic flow rule coupled with linear isotropic hardening cannot describe all stages of salt specimen deformation. Due to the dislocation nature this criterion underestimates the transverse deformations. Obviously, salt rocks show dilatant effects, which are not reflected by Tresca yield criterion.

To account dilatancy, pressure-sensitive strength criteria are used. The considered classical linear Mohr-Coulomb criterion allows us to describe accurately all stages of deformation during loading of the specimen. Nevertheless, the associated plastic flow rule leads to excessive transverse deformations. However, application of the non-associated flow rule with the additional parameter (the dilatancy angle) enables us to control the level of transverse deformations. Therefore, both the loading and the transverse deformations curves of salt specimen can be accurately described.

The parabolic analogue of the linear Mohr-Coulomb strength criterion—the parabolic envelope of Mohr circles (PMC)—has no physical sense for a certain range of principal stresses. Therefore, for practical application, PMC can be complemented by the Rankine criterion (PMC/R). Also, in the PMC model, isotropic linear hardening can be incorporated similar to the Tresca criterion. The resulting loading diagram for the PMC/R criterion with the associated law of plastic flow and linear isotropic hardening describes the test curve qualitatively well. However, as for the linear Mohr-Coulomb criterion with associated flow rule, the transverse deformations of the cubic salt specimen are excessive. In contrast to the linear analogue, the constraint of transverse deformations here has no physical sense.

The volumetric strength criterion [23] for rocks compared to PMC physically correctly describes all ranges of principal stresses. Moreover, the yield function is continuously differentiable over the entire principal stress space. It significantly simplifies the calculation of plastic strain in their associated flow. The test loading diagram can be accurately described only with the hardening effect. The linear isotropic hardening allows us to obtain a loading curve close enough to the test one for the associated volumetric yield criterion. Furthermore, the simulated loading diagrams of the PMC/R and [23] criteria nearly coincide. However, in contrast to all considered criteria, the volumetric yield criterion can be considered as the most accurate for the description of transverse deformations over the specimen cross section.

Acknowledgement

The work was supported by the Russian Science Foundation (grant no. 19-77-30008)

References

[1] Baryakh, A.A., Konstantinova, S.A. and Asanov, V.A. (1996). Rock Salt Deformation. Yekaterinbug, UB of RAS.

[2] Fahland; S., Hammer, J., Hansen, F., et al. (2018). The Mechanical Behavior of Salt IX / Proceedings of the 9th Conference on the Mechanical behavior of salt. SaltMech IX, Hannover, Germany.

[3] He, M.M., Ren, J., Su, P. et al. (2020). Experimental Investigation on Fatigue Deformation of Salt Rock. Soil Mech Found Eng, 56, pp. 402–409. DOI: 10.1007/s11204-020-09622-x.

[4] Dubey, R.K. and Gairola, V.K. (2000). Influence of structural anisotropy on the uniaxial compressive strength of pre-fatigued rocksalt from Himachal Pradesh, India, International Journal of Rock Mechanics and Mining Sciences, 37(6), pp. 993-999. DOI: 10.1016/S1365-1609(00)00020-4.

[5] Baryakh, A.A., Lobanov, S.Y. and Lomakin, I.S. (2015). Analysis of time-to-time variation of load on interchamber pillars in mines of the Upper Kama Potash Salt Deposit, J Min Sci, 51, pp. 696–706. DOI: 10.1134/S1062739115040064.

[6] Pałac-Walko, B. and Pytel, W. (2019). Geomechanical risk assessment for saltrock underground workings, using strength theories based on selected 2D and true 3D triaxial compression laboratory tests, SGEM 19(1.3), pp. 307-314. DOI: 10.5593/sgem2019/1.3/S03.039.

[7] Wang, Q. and Hesser, J. (2013). Determination of the deformation behaviour of salt rock by evaluation of convergence measurements in shafts, Paper presented at the ISRM SINOROCK 2013, Shanghai, China, 18-20 June.

[8] Heusermann, S., Rolfs, O., and Schmidt, U. (2003). Nonlinear finite-element analysis of solution mined storage caverns in rock salt using the LUBBY2 constitutive model, Computers and Structures, 81(8-11), pp. 629-638. DOI: 10.1016/S0045-7949(02)00415-7.
[9] Hou, Z. (2003). Mechanical and hydraulic behavior of rock salt in the excavation disturbed zone around underground facilities, International Journal of Rock Mechanics and Mining Sciences, 40(5), pp. 725-738. DOI: 10.1016/S1365-1609(03)00064-9.
[10] Baryakh, A.A., Eremina N.A. and Gracheva E.A. (1994). Crack development in disturbed salt bed, J. Min. Sci., 30(5), pp. 487-490. DOI: 10.1007/BF02047340
[11] Ulusay, R. ed., (2015). The ISRM Suggested Methods for Rock Characterization, Testing and Monitoring: 2007–2014, Switzerland, Springer Cham. DOI: 10.1007/978-3-319-07713-0.
[12] You, M. (2011). Comparison of the accuracy of some conventional triaxial strength criteria for intact rock, IJRMMS, 48(5), pp 852-863. DOI: 10.1016/j.ijrmms.2011.05.006.
[13] Labuz, J.F., Zang, A. (2012). Mohr–Coulomb Failure Criterion, Rock Mech Rock Eng, 45, pp. 975–979. DOI: 10.1007/s00603-012-0281-7.
[14] Wang, D.J., Tang, H., Shen, P., Cai, Y. (2019). A Parabolic Failure Criterion for Transversely Isotropic Rock: Modification and Verification, Mathematical Problems in Engineering, 2019. DOI: 10.1155/2019/8052560.
[15] Baryakh, A. A., Samodelkina N. A. and Pan'kov I.L. (2012). Water-tight stratum failure under large-scale mining. Part I., J. Min. Sci., 48(5), pp. 771-780. DOI: 10.1134/S1062739148050012.
[16] Baryakh, A.A., Evseev, A.V., Lomakin, I.S., Tsayukov, A.A. (2020). Operational control of rib pillar stability, Eurasian Mining, 2020(2), pp. 7-10. DOI: 10.17580/em.2020.02.02.
[17] Baryakh, A.A., Tsayukov, A.A., Evseev, A.V. et al. (2021). Mathematical Modeling of Deformation and Failure of Salt Rock Samples, J. Min. Sci. 57(3), pp. 370–379. DOI: 10.1134/S1062739121030029.
[18] de Souza Neto, E.A., Perić, D. and Owen, D.R.J. (2008). Computational Methods for Plasticity: Theory and Applications, Chichester, John Wiley & Sons Ltd. DOI: 10.1002/9780470694626.
[19] Zienkiewicz, O.C., Taylor, R.L. and Fox, D. (2014). The Finite Element Method for Solid and Structural Mechanics (7th edition), Butterworth-Heinemann. DOI: 10.1016/C2009-0-26332-X.
[20] de Borst, R., Crisfield, M.A., Remmers, J.J.C., Verhoosel, C.V. (2012). Non-Linear Finite Element Analysis of Solids and Structures, 2nd Edition, Chichester, John Wiley & Sons Ltd. DOI: 10.1002/9781118375938.
[21] Ottosen, N.S., Ristinmaa, M. (1996). Corners in plasticity—Koiter's theory revisited, IJSS, 33(25), pp. 3697-3721. DOI: 10.1016/0020-7683(95)00207-3.
[22] Rankine, W.J.M. (1877). A manual of applied mechanics, 9 ed, London, Charles Griffin and company.
[23] Baryakh, A.A. and Samodelkina N.A. (2017). About one criteria of strength of rocks, Chebyshevskii Sbornik, 18(3), pp. 72-87. DOI: 10.22405/2226-8383-2017-18-3-72-87.